Biosensors and Bioelectronics 162 (2020) 112234

Contents lists available at ScienceDirect

Biosensors and Bioelectronics

journal homepage: http://www.elsevier.com/locate/bios

Synthesis of a PEDOT-TiO_2 heterostructure as a dual biosensing platform operating *via* photoelectrochemical and electrochemical transduction mode

Hejie Zheng [a], Si Zhang [a], Xiaoqiang Liu [a,**], Yanmei Zhou [a], Subbiah Alwarappan [b,*]

[a] Henan Joint International Research Laboratory of Environmental Pollution Control Materials, College of Chemistry and Chemical Engineering, Henan University, Kaifeng, 475004, PR China

[b] Electrodics and Electrocatalysis Division, CSIR-Central Electrochemical Research Institute, Karaikudi, 630003, Tamil Nadu, India

ARTICLE INFO

Keywords:
Poly (3,4-dioxoethylthiophene)
TiO_2 nanowire arrays
Lactate dehydrogenase
Coenzyme NAD^+
Photoelectrochemical and electrochemical sensing

ABSTRACT

A new organic-inorganic heterostructure was prepared by the hydrothermal deposition of poly (3,4-dioxoethylthiophene) (PEDOT) on TiO_2 nanowire arrays (TiONWs) to construct a biosensor that can simultaneously function as photoelectrochemical (PEC) and electrochemical (EC) sensor to detect lactate. In both cases, the PEDOT-TiONWs heterostructure not only acted as an immobilization platform for lactate dehydrogenase (LDH) and coenzyme NAD^+, but also generated current signals, which were further amplified by the cyclic catalytic mechanism. Specifically, LDH catalytically converted lactate to pyruvate, meanwhile NAD^+ was transformed to NADH. For PEC sensing, the photo-generated holes from PEDOT-TiONWs could oxidize NADH back to NAD^+, fulfilling a catalytic cycle. Herein, PEDOT significantly promoted the separation of electron-hole pairs and enhanced PEC signals due to its well-matched energy levels with TiONWs, high conductivity and strong visible light absorption. A dynamic range of 0.5–300 μM was observed between the PEC signals and lactate concentration, based on which a sensitivity of 0.1386 ± 0.0053 μA μM^{-1} and a detection limit of 0.08 ± 0.0032 μM were estimated. For EC sensing, PEDOT-TiONWs could directly oxidize NADH to NAD^+ at ~0.54 V to realize the cyclic amplification due to the high conductivity and strong electrocatalytic capability of the heterostructure. The EC biosensor displayed a similar performance upon PEC mode of operation, except the relatively poor selectivity due to the possible oxidation of the interferences at the potentials > 0.54 V.

1. Introduction

The performance of PEC and EC biosensors are extremely dependent on the property of the materials modified on sensor surface. As a result, the exploitation of new materials with special PEC or/and EC features is of great significance for the further improvement of PEC and EC biosensing (Cheng et al., 2018; Gao et al., 2020). Till date, majority of the materials employed in PEC and EC sensing are inorganic semiconductors, which are inferior to conducting polymers in the aspects of electrical conductivity, tuning of band position and width, porousness and specific surface area (Ghosh et al., 2018; He et al., 2019; Rajesh et al., 2017; Wang et al., 2010). For example, conducting polymers such as polythiophene, polyaniline, polypyrrole and poly (3,4-ethylenedioxythiophene) (PEDOT) were extensively employed for electrocatalysis and photocatalysis due to their high conductivity and large conjugated π bonds in their molecular backbone (Ghosh et al., 2014; Kim et al., 2020; Łapkowski and Proń, 2000; Lv et al., 2019; Shao et al., 2018). Especially, PEDOT is one of the most ideal materials in energy storage devices, solar cells, electrochemical sensors and electrochromic dispaly, etc. due to its superior conductivity (over conducting polymers), good flexibility, large surface area, exciting bandgap (~1.5 eV), facile synthesis and high stability (Chong et al., 2017; Rajesh et al., 2017). However, till date, there are only a few reports on the application of PEDOT in PEC and EC biosensing.

During the synthesis, severe aggregation of PEDOT usually results in the significant loss in its conductivity, optical capability and specific surface area (Madhuvilakku et al., 2020; Rajesh et al., 2017). Therefore, it is an ideal strategy to grow conducting polymers on inorganic semiconductors to alleviate their aggregation and the associated issues. The formation of composite not only favors the simple functions of the individuals, but also generate the optical-electrical synergistic effect, which may improve the overall performance of the materials (Jiang

* Corresponding author.
** Corresponding author.
E-mail addresses: liuxq@henu.edu.cn (X. Liu), salwarap@gmail.com (S. Alwarappan).

https://doi.org/10.1016/j.bios.2020.112234
Received 2 March 2020; Received in revised form 11 April 2020; Accepted 21 April 2020
Available online 4 May 2020

et al., 2013; Madhuvilakku et al., 2020).

Amongst the widely employed metal oxide nano-semiconductors, TiO_2 is widely preferred for EC and PEC biosensing due to its easy preparation protocol, availability in diverse forms, good stability, high photocatalytic activity and excellent biocompatibility (Zhang et al., 2014; Zhu et al., 2016). In particular, one-dimensional TiO_2 nanostructures displayed a band gap of 3.0 eV and lower electron-hole recombination rate compared with other TiO_2 nanostructures (Chen et al., 2010; Wang et al., 2011; Yang et al., 2019). In order to improve the optical and electrical properties, it is essential to combine TiO_2 with other materials to form composites. For example, polythiophene/Pd/TiO_2 ternary composite microspheres were employed to design a PEC sensor for the detection of L-cysteine. Due to the high surface area, effective charge transfer and enhanced light absorption of the ternary composite, the PEC sensor displayed superior sensitivity, selectivity and stability over the traditional electrochemical sensors with a detection limit of 9.24 μM and a linear range of 0.31–5.30 mM (Wang et al., 2014).

Lactic acid, a α-hydroxy acid obtained from pyruvate, plays a key role in several biochemical processes and its detection is highly useful in food analysis, clinical analysis and fermentation industry (Dong et al., 2019; Lei et al., 2012; Piano et al., 2010; Zhao et al., 2015). The routine lactic acid detection includes spectrophotometry (Parra et al., 2006; Teymourian et al., 2012; Tsai et al., 2007), colorimetry (Celik et al., 2015), chromatography (Rathee et al., 2016; Zhao et al., 2014), refractive index (Nesakumar et al., 2014) and capillary electrophoresis (Monošík et al., 2012). To achieve a fast, selective and sensitive detection of lactic acid or lactate, a few PEC and EC biosensors based on lactate oxidase (LOD) or lactate dehydrogenase (LDH) have been developed. For example, lactate oxidase modified ZnO nanorods were used as potentiometric biosensor for the lactate analysis. This biosensor exhibited high selectivity and stability towards lactate with a linear detection range of 0.001–1 mM and a sensitivity of ~41.33 ± 1.58 mV/decade (Ibupoto et al., 2012).

In the present work, a multi-functional PEDOT-TiONWs composite was synthesized to construct a single biosensor for both PEC and EC sensing. The comparison between the working mechanism and performance of these two sensing techniques were performed and discussed in detail. The construction procedure of the biosensor is described in Scheme 1. Firstly, TiO_2 nanowire arrays were synthesized on FTO glass substrates by a hydrothermal method to produce TiONWs|FTO, on which PEDOT was then hydrothermally grown to obtain PEDOT-TiONWs|FTO. After acidified with MPA, PEDOT-TiONWs|FTO acted as a platform for immobilizing LDH and NAD^+ *via* an amide bond to obtain the biosensor for the detection of lactate by both PEC and EC routes. The only difference between the PEC and EC biosensing is the catalytic reaction mechanism for the signal amplification. For the PEC biosensing, NADH was oxidized by the photo-generated holes to regenerate NAD^+, while NAD^+ was reproduced by the direct EC oxidation of NADH on PEDOT-TiONWs|FTO for EC biosensing. The recycling of NAD^+ and special features of PEDOT-TiONWs significantly amplified the current signals at the as-prepared PEC and EC biosensors.

2. Experimental

2.1. Material and reagents

Commercial fluorine-doped tin oxide (FTO) glasses (1.6 mm thickness, 14 Ω/sq sheet resistance) were obtained from Wuhan Lattice Solar Energy Technology, Ltd., China. Concentrated hydrochloric acid (37 wt %), concentrated sulfuric acid (97 wt%) and tetrabutyl titanate were ordered from Tianjin Chemical Reagent Co., Ltd., China. Ammonium persulfate (98%) was purchased from J&K Scientific, Ltd., Beijing, China. LDH, NADH, β-NAD^+ hydrate and sodium L-lactate (98%) were all purchased from Sigma-Aldrich Co. (St. Louis, MO, USA). Ultrapure water (≥18 MΩ cm^{-1}) obtained from a Millipore water purification system was used all through the experiment. N-(3-dimethylaminopropyl)-N′-ethylcarbodiimide hydrochloride (EDC), N-hydroxy succinimide (NHS), 3,4-ethylenedioxythiophene (EDOT) monomer (99% purity) and 3-mercaptopropionic acid (MPA) were purchased from Macklin Chemistry Co. Ltd., China. Phosphate buffered saline (PBS, pH 7.4) was prepared with the stock solutions of 0.1 M KH_2PO_4, K_2HPO_4 and KCl.

2.2. Apparatus

All EC and PEC measurements were conducted at a CHI630C electrochemical workstation (Shanghai, CH Instruments, China) with a three-electrode system in 0.1 M PBS. An Ag|AgCl electrode (3.0 M KCl), a platinum wire and a modified FTO electrode were used as the reference electrode, auxiliary electrode and working electrode respectively. Electrochemical impedance measurements were performed at an IM6ex

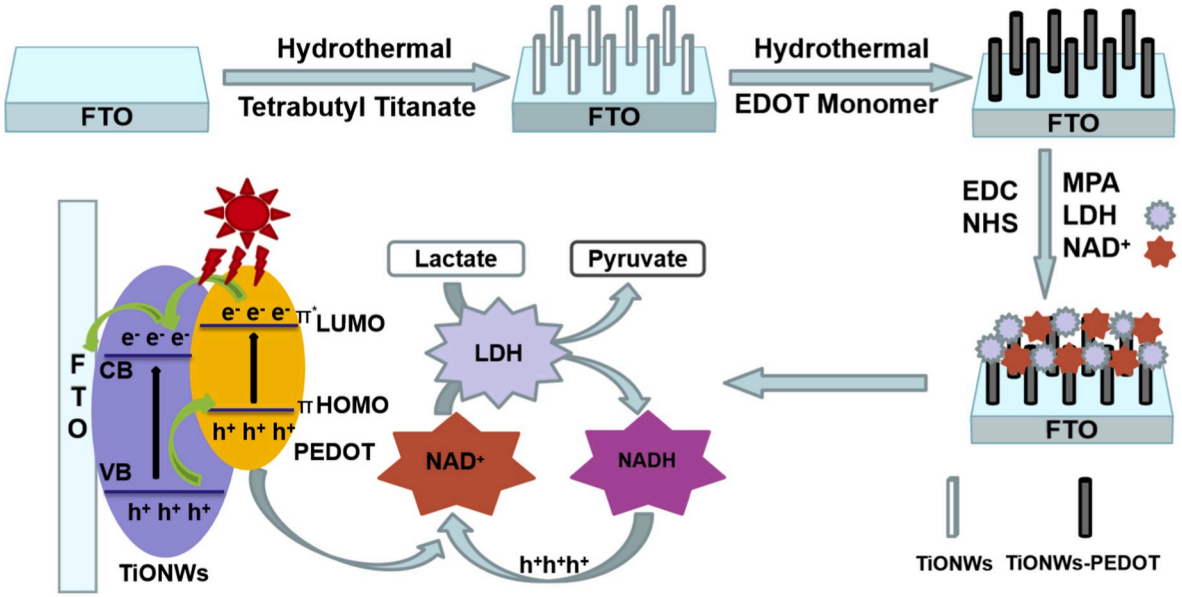

Scheme 1. Schematic diagram of preparation and reaction mechanism of the PEC biosensor.

electrochemical work station (ZAHNER, Germany). A Xe lamp equipped with a 400 nm cut-off filter was employed as the visible light source (CEL-HXUV 300, Beijing AULTT, China) in the PEC detection system. The morphology and chemical composition of the materials were characterized by a field emission scanning electron microscopy (SEM, JSM-7500 F, JEOL., Japan) and a X-ray photoelectron spectrometer (ESCALAB 250Xi, USA) with a monochromatic Al Kα source (hν = 1486.6 eV, 150 W power, 500 μm beam spot). The obtained XPS spectra were calibrated on the C1s peak (284.8 eV) and analyzed by XPSPEAK41 software. X-ray diffraction spectrometer (XRD, Bruker D8 Advance, Germany) with a Cu Kα radiation was used to verify the crystal forms of the prepared materials. The organic polymer was characterized using Fourier transform infrared spectrometer (FT-IR, Nicolet 170, USA). UV–vis diffuse reflectance spectra of the samples were acquired using an UV–vis spectrophotometer (DRS, UV-2600, Kyoto, Japan).

2.3. Preparation of TiONWs|FTO

Rutile TiO_2 nanowire arrays were successfully synthesized on FTO glass substrates by a hydrothermal method (Cui et al., 2019; Liu et al., 2017b). Before the reaction, FTO glass substrates were washed successively with toluene, acetone, ethanol and deionized water in an ultrasonicator for 15min each, and dried under N_2 stream for later use. Later, 12.5 mL of Con. HCl and 12.5 mL deionized water was mixed. To this, 400 μL of tetrabutyl titanate was slowly added and stirred for 20 min to obtain a clear solution. Subsequently, the mixed solution and the cleaned FTO substrates were transferred into a 100 mL Teflon lined stainless-steel autoclave, and the hydrothermal reaction was maintained at 180 °C for 5 h. After the autoclave was cooled to room temperature, the modified FTO substrates were taken out, washed with deionized water and dried under N_2 stream. The FTO substrates covered with white uniform film of TiO_2 nanowire arrays were eventually annealed at 500 °C for 2 h at an annealing rate of 5 °C min^{-1}.

2.4. Preparation of PEDOT-TiONWs|FTO

At room temperature, 27 μL of EDOT monomer was added to 30 mL 0.2 M H_2SO_4, which was stirred for 20 min for uniform dispersion of EDOT monomer. To this, 0.056 g APS was added and continuously stirred for 1 h. Then, the above solution and the prepared TiONWs|FTO substrate were transferred into a 50 mL Teflon lined stainless-steel autoclave, and reacted at 150 °C for 5 h. After being cooled down to room temperature, the PEDOT-TiONWs|FTO substrate was taken out, washed with deionized water and ethanol, and dried at 60 °C for 12 h. It was clearly observed that the white TiONWs|FTO turned black after the deposition of PEDOT. Pure PEDOT was also prepared using the same protocol as above for control.

2.5. Construction of the LDH biosensor

The LDH biosensor was fabricated as follows. Initially, the PEDOT-TiONWs|FTO electrode was acidified using 10 mM MPA at 4 °C for 2 h, and the excess MPA was washed off with 0.1 M PBS (pH 7.4). Then, the acidified PEDOT-TiONWs|FTO electrode was soaked in 0.1 M PBS containing 10 mM EDC and 20 mM NHS for 2 h to activate the free carboxyl groups at the surface of the electrode. After excess EDC and NHS were thoroughly washed off with 0.1 M PBS, 50 μL of 5 mg mL^{-1} LDH in 0.1 M PBS was applied to the modified electrode surface, and incubated at 4 °C for 3 h. Following that, 50 μL of 15 mM NAD^+ in 0.1 M PBS was added to the LDH modified electrode surface, and dried at 4 °C overnight. Subsequently, the obtained NAD^+|LDH|PEDOT-TiONWs|FTO was washed with 0.1 M PBS and stored at 4 °C.

3. Results and discussion

3.1. SEM and EDX analysis of the prepared materials

The surface morphology and the appearance of the as prepared samples were characterized by SEM. The front and side views of bare TiONWs (Fig. 1A and the left image in Fig. 1D and E) indicated that a layer of dense, uniform and vertical nanowire arrays with a rectangular cross-section had successfully grown on the FTO surface following a hydrothermal treatment. The average diameter and length of TiONWs were estimated to be ~110–200 nm and ~1.5–2.0 μm, respectively. As reported previously, pure PEDOT (Fig. 1B) displayed an amorphous structure without any definite morphology (Li et al., 2018; Rajesh et al., 2016a; Rajesh et al., 2017). It is evident that the head of pure TiONWs is coarse and uneven (the left image in Fig. 1D). In comparison, a thick layer of uniform film was immobilized on TiONWs surface after the hydrothermal deposition of PEDOT, as shown by the right image in both Fig. 1D and E. Consequently, Fig. 1D and E could be used as the evidence for the successful preparation of PEDOT-TiONWs composite. Furthermore, the elemental composition of PEDOT-TiONWs was analyzed from the energy dispersive X-ray pattern shown in Fig. 1F. Besides the Sn peaks attributed to the FTO substrate, the peaks of Ti, O, C and S elements were also identified in the EDX spectrum of PEDOT-TiONWs, which could be used as another evidence for the formation of the composite.

3.2. XPS characterization of the PEDOT-TiONWs composite

XPS survey spectrum (Fig. 2A) showed the Ti 2p, C 1s, O 1s and S 2p peaks and all these belong to the typical XPS peaks of PEDOT-TiONWs composite. As shown in Fig. 2B, two typical Ti^{4+} $2p_{3/2}$ and Ti^{4+} $2p_{1/2}$ peaks are observed at 458.56 and 464.64 eV respectively, indicating the presence of TiO_2 (Dong et al., 2017; Li et al., 2019; Liu et al., 2017b; Wang et al., 2018a). Moreover, the noise on the Ti 2p curves may be ascribed to the dense coverage of TiONWs by PEDOT. Fig. 2C displayed that the C 1s peak could be de-convoluted into three peaks at 284.57, 285.80, and 287.91 eV and they correspond to the C═C, C–C, and C–O/C–S bonds of PEDOT respectively (Lei et al., 2019; M and Berchmans, 2019; Munusamy et al., 2019; Wu et al., 2019). As shown in Fig. 2D, the characteristic O 1s peaks at 530.54 eV, 531.91, and 533.29 eV corresponds to the lattice oxygen [Ti–O_6] of TiONWs, the Ti–OH groups on the surface of TiONWs and the carboxyl group (C–O) in PEDOT respectively (Li et al., 2019; Liu et al., 2017b; Madhuvilakku et al., 2020). In the XPS spectrum of the S element (Fig. 2E), the S 2p peaks could be fitted as S $2p_{3/2}$ and S $2p_{1/2}$ peaks at 163.73 and 164.92 eV respectively, which can be ascribed to the PEDOT thiophene ring (Guo et al., 2020; Ling et al., 2019; Munusamy et al., 2019; Zeng et al., 2019). In summary, the above XPS results demonstrated that the PEDOT had successfully grown on TiONWs to form PEDOT-TiONWs composite.

3.3. FT-IR analysis of the prepared materials

FT-IR spectroscopic measurements were performed to confirm the synthesis of the materials by identifying their typical functional groups in the spectra. As presented in Fig. 3A, a wide peak band of 3000–3700 cm^{-1} and a peak at 1632 cm^{-1} are the respective stretching and in-plane bending vibration of –OH groups present on the surface of the prepared materials (Madhuvilakku et al., 2020). The absorption peaks at 657 cm^{-1} and 429 cm^{-1} (trace a) belong to the Ti–O stretching vibration and Ti–O–Ti bridging vibration (Zhu et al., 2016). In the FT-IR spectrum of pure PEDOT (trace b), the spectral vibration bands at 1515 cm^{-1} and 1351 cm^{-1} are ascribed to the C═C and C–C stretching vibration of quinonoid structure in thiophene rings, respectively (Ghosh et al., 2018; Gupta et al., 2018; Rajesh et al., 2016b; Rajesh et al., 2017). The peaks at 983, 844 and 696 cm^{-1} corresponds to the C–S stretching vibrations of thiophene rings, and the absorption bands at 1211, 1140 and 1096 cm^{-1}

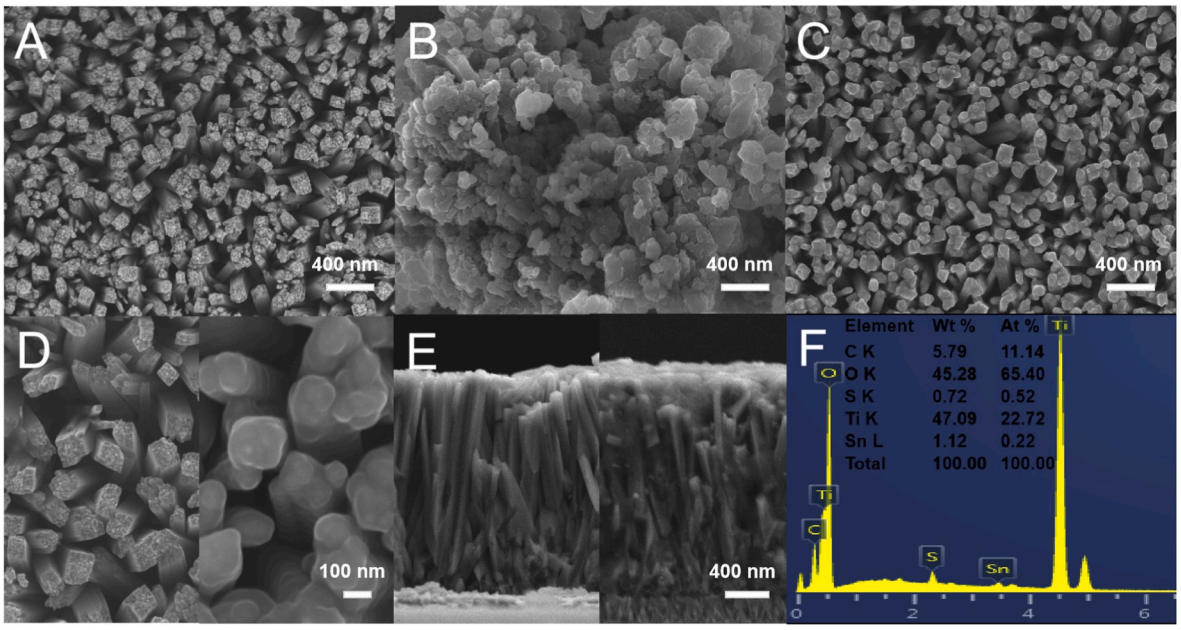

Fig. 1. SEM images of (A) bare TiONWs; (B) pure PEDOT; (C) PEDOT-TiONWs composite; (D) enlarged views of bare TiONWs (left) and PEDOT-TiONWs composite (right); (E) side views of bare TiONWs (left) and TiONWs-PEDOT composite (right); (F) EDX patterns of TiONWs-PEDOT composite.

are attributed to the C–O–C bending vibrations of ethylenedioxy group (Chen et al., 2017; Ghosh et al., 2014; Guo et al., 2020; Li et al., 2018; Madhuvilakku et al., 2020). Most importantly, all the characteristic absorption bands of TiO_2 and PEDOT are observed in the FT-IR spectrum of PEDOT-TiONWs composite (trace c). Moreover, the intensity of Ti–O stretching vibration and Ti–O–Ti bridging vibration at 655 cm^{-1} and 433 cm^{-1} has significantly decreased due to the complete coverage of PEDOT on TiONWs. All the above results confirmed the formation of PEDOT on TiO_2 by the hydrothermal strategy.

3.4. XRD characterization of the prepared materials

XRD patterns of FTO, TiONWs|FTO, PEDOT and PEDOT-TiONWs|FTO are shown in Fig. 3B. On curve a, the characteristic peaks at 26.51°, 34.01°, 38.01°, 51.81°, 54.92°, 61.73° and 65.72° belong to SnO_2 on bare FTO substrate (Liu et al., 2017b; Yang et al., 2019). On curve b, the characteristic peaks at 36.18° and 62.92° correspond to the (101) and (002) crystal planes of the crystalline rutile TiONWs (Wang et al., 2018a; Zhang et al., 2014). The XRD pattern of PEDOT (curve c) shows a typical wide peak at ~26.08°, attributed to the inter-molecular π-π* stacking from the (020) reflection of polymer backbone (Lei et al., 2019; Madhuvilakku et al., 2020). The XRD pattern of PEDOT-TiONWs|FTO (curve d) shows almost all the diffraction peaks of TiONWs, PEDOT and FTO, demonstrating the successful preparation of PEDOT-TiONWs composite. However, the typical (020) peak of PEDOT at ~26.08° overlap with that of SnO_2 on the FTO substrate (Chong et al., 2017).

3.5. UV–visible diffuse reflectance spectra of the prepared materials

As shown in Fig. 3C, the optical absorption property of TiONWs|FTO, pure PEDOT and PEDOT-TiONWs|FTO composite were studied by UV–visible diffuse reflectance spectroscopy. TiONWs (curve a) displays strong absorption only in the UV region with an absorption edge at ~410 nm. According to the Scherer equation the bandgap (E_g) of TiONWs was estimated to be ~3.02 eV, which was consistent with the previous report (Liu et al. 2017a, 2017b). On the contrary, pure PEDOT (curve b) showed intense absorption on the whole UV–vis region from 300 to 800 nm due to its long chain conjugation structure (Ghosh et al. 2014, 2018; Janaky et al., 2010; Rajesh et al., 2016b; Samu et al., 2015). Most importantly, PEDOT-TiONWs composite (curve c) can also absorb both UV and visible light, just like PEDOT polymer. In particular, the broad band at 430–800 nm is attributed to the bipolaron subgap transitions of PEDOT. The above results demonstrated the formation of PEDOT-TiONWs composite with strong visible light absorption, which is necessary for constructing visible light PEC sensor.

3.6. EIS characterization of the LDH biosensor assembly

EIS was used to characterize the LDH biosensor (Tang et al., 2018; Wang et al., 2018b). The EIS test was performed in 5.0 mM $[Fe(CN)_6]^{3-}$/$[Fe(CN)_6]^{4-}$ in 0.1 M KCl at a 0.23 V DC voltage superimposed by an AC voltage of 5 mV in the 100 kHz-0.1 Hz frequency range. It has been reported that the diameter of the semicircle in a Nyquist plot represents the electron transfer resistance (R_{et}), and the straight line in the low frequency region represents the diffusion control process (Shuai et al., 2016). As shown in Fig. 3D, FTO substrate (curve a) displays a semi-circle with smallest diameter among all the modified electrodes, corresponding to a near diffusion control process. In contrast, the diameter of the semi-circle corresponding to TiONWs|FTO electrode (curve b) is the largest among these electrodes, indicating a large electron transfer resistance and poor conductivity on TiONWs|FTO. However, upon the deposition of a uniform layer of PEDOT on TiONWs|FTO surface (curve c), the R_{et} of the electrode was significantly reduced by ~62%, compared with that of TiONWs|FTO (curve b). This could be attributed to the formation of heterojunction, which facilitated the electron transfer of $[Fe(CN)_6]^{3-/4-}$ on electrode surface. After the immobilization of LDH and NAD^+, the diameter of the semicircle (curve d) increased significantly relative to the PEDOT-TiONWs|FTO (curve c) due to the presence of the large biomolecules that obstructed the electron transfer on electrode surface, which also confirmed the successful immobilization of LDH and NAD^+ on PEDOT-TiONWs|FTO surface. In summary, the significant change noticed with the R_{et} values in Fig. 3D indicated the sequential modification of the materials and biomolecules on the FTO substrate for the successful construction of the LDH biosensor.

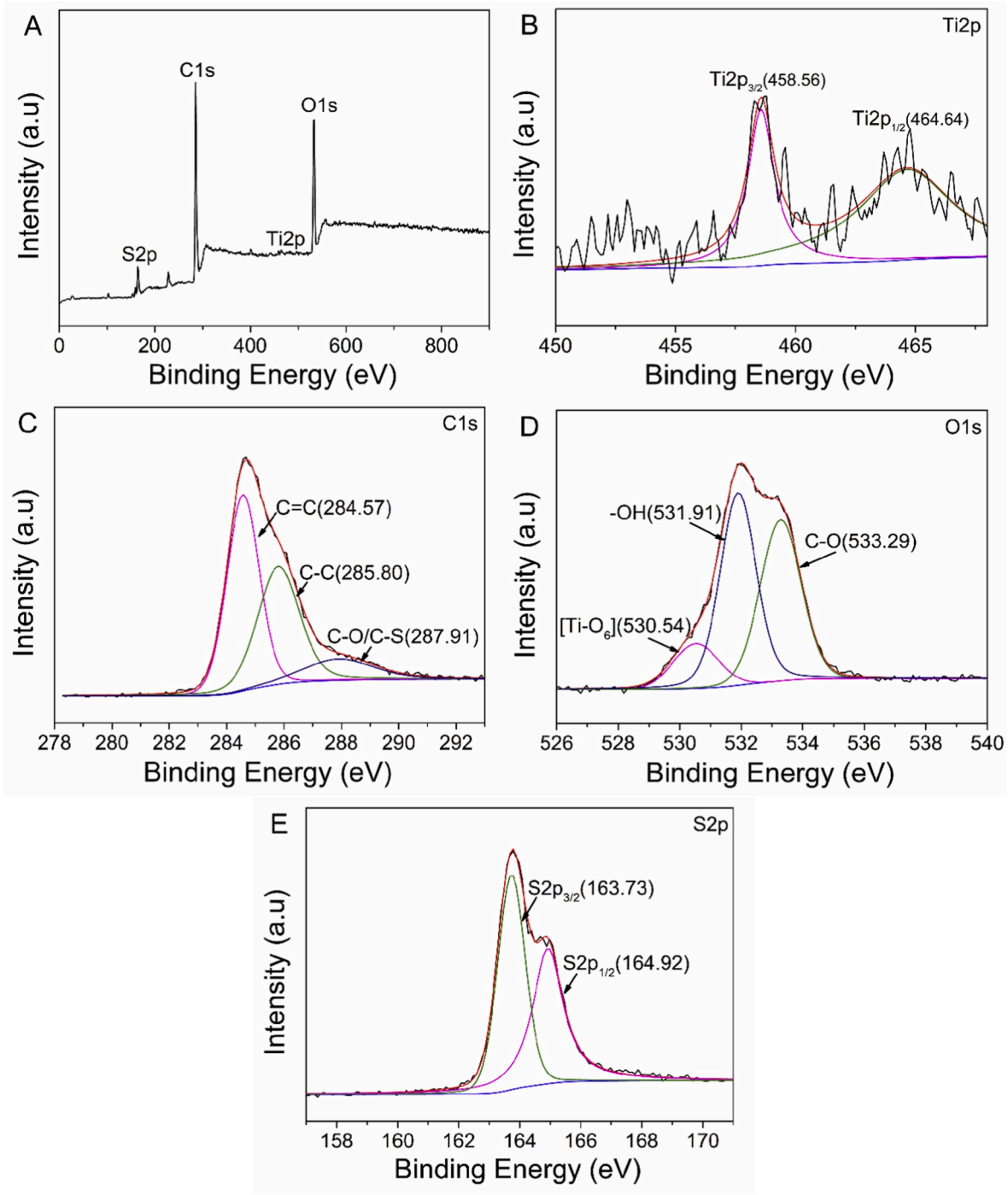

Fig. 2. XPS analysis of PEDOT-TiONWs composite: (A) XPS survey spectrum, and the corresponding high resolution XPS spectra of (B) Ti 2p, (C) C 1s, (D) O 1s, (E) S 2p.

3.7. Electrochemical investigation of the LDH biosensor

Cyclic voltammetry was performed to investigate the electrochemical behavior of the LDH biosensor, as shown in Fig. 4A. Regardless the absence or presence of L-lactate, PEDOT-TiONWs|FTO showed a nearly featureless voltammogram (curves a, b) within the potential range of −0.2 to +1.0 V, mainly due to the electrochemical inertness of TiONWs. Though there was a small amount of PEDOT on TiONWs, the Faradaic component from PEDOT was masked by the excess charging current. Therefore, PEDOT-TiONWs composite exhibited a significant electrochemical interference to the detection of L-lactate. On the contrary, NAD^+|LDH|PEDOT-TiONWs|FTO exhibited a significant anodic peak (vs Ag|AgCl) at ~0.54 V in the presence of 100 μM L-lactate (curve d) due the strong oxidation capability of PEDOT-TiONWs towards NADH. The mechanism of EC biosensing follows equations (1) and (2). Similar to the PEC biosensing, LDH transformed lactate to pyruvate, while NAD^+ was reduced to NADH, which was then oxidized by the modified electrode to regenerate NAD^+. Accordingly, the increase in the L-lactate concentration will enhance the electrocatalytic current, which indirectly realized the quantitative determination of lactate.

$$\text{Lactate} + NAD^+ \xrightarrow{LDH} \text{Pyruvate} + NADH + H^+ \quad \text{Equation 1}$$

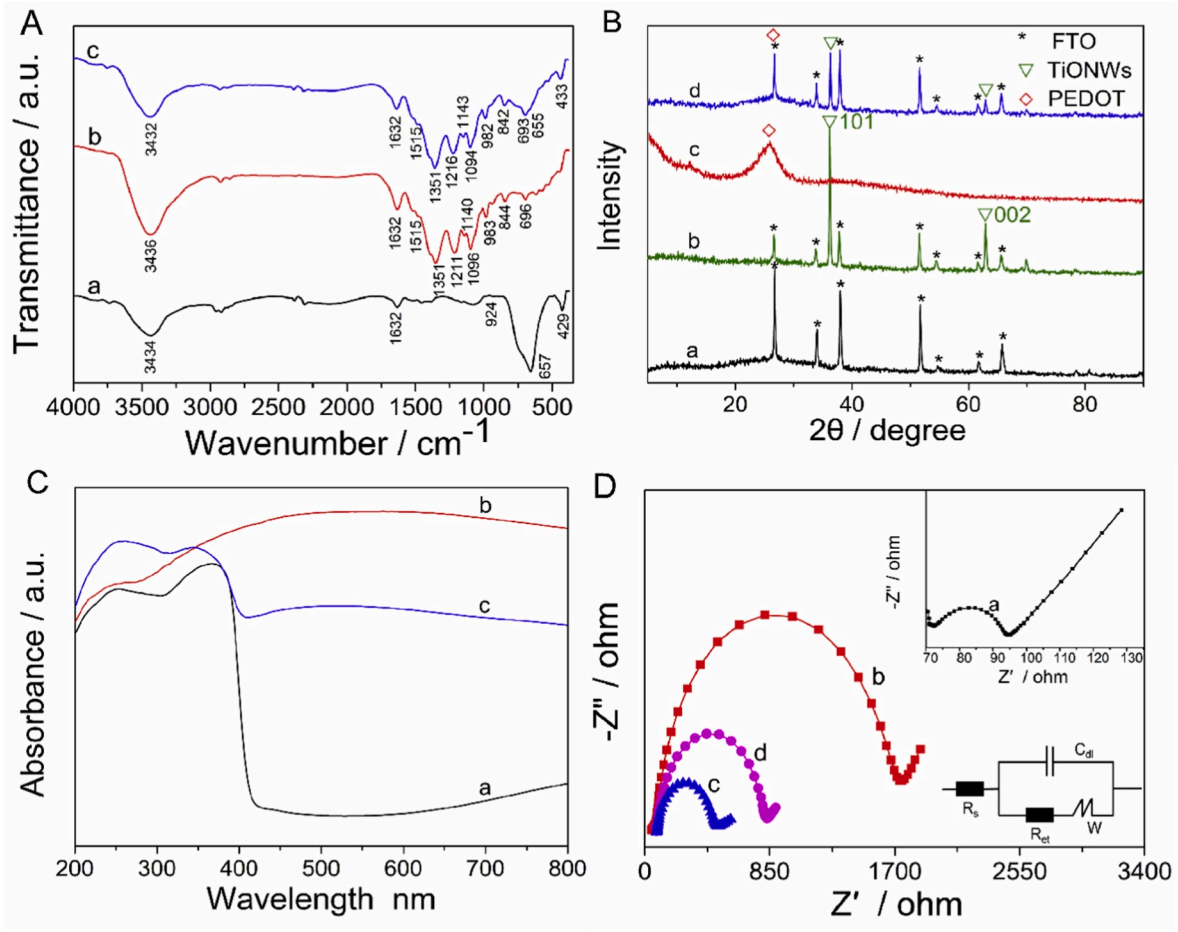

Fig. 3. (A) FT-IR spectra of (a) TiONWs, (b) PEDOT, (c) PEDOT-TiONWs; (B) XRD patterns of (a) FTO substrate, (b) TiONWs|FTO, (c) pure PEDOT and (d) PEDOT-TiONWs|FTO; (C) UV–vis diffuse reflectance spectra of (a) TiONWs|FTO, (b) pure PEDOT and (c) PEDOT-TiONWs|FTO; (D) Nyquist plot of (a) FTO, (b) TiONWs|FTO, (c) PEDOT-TiONWs|FTO, (d) NAD+|LDH|PEDOT-TiONWs|FTO.

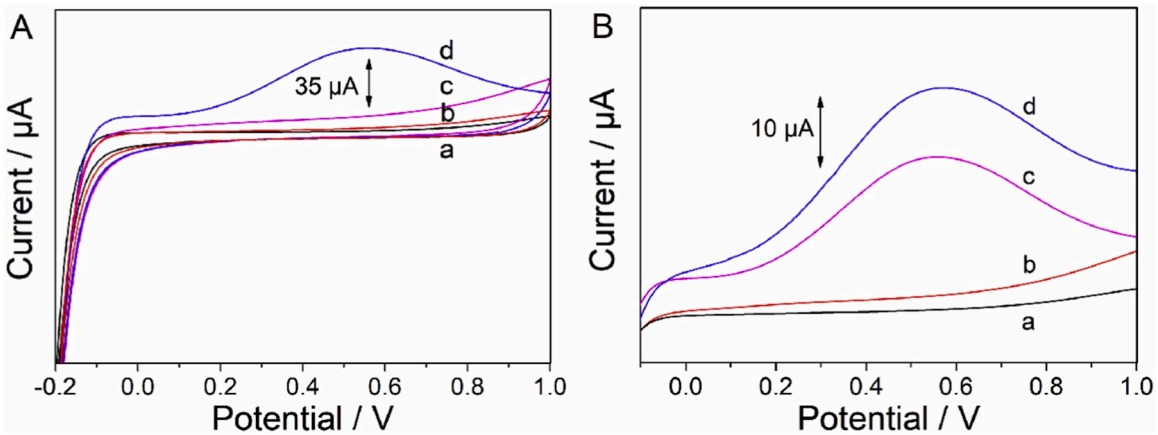

Fig. 4. (A) Cyclic voltammograms of PEDOT-TiONWs|FTO in the absence (a) and presence (b) of 100 μM L-lactate, and of NAD^+|LDH|PEDOT-TiONWs|FTO in the absence (c) and presence (d) of 100 μM L-lactate in 0.1 M PBS (pH = 7.4) at a scan rate of 50 mV s^{-1}; (B) Linear scan voltammograms of PEDOT-TiONWs|FTO in the presence of 100 μM L-lactate without (a) and with (b) illumination, NAD^+|LDH|PEDOT-TiONWs|FTO in the presence of 100 μM L-lactate without (c) and with (d) illumination in 0.1 M PBS (pH = 7.4) at a scan rate of 50 mV s^{-1}.

$$NADH - 2e^- \xrightarrow{\text{electrochemical oxidation}} NAD^+ + H^+ \qquad \text{Equation 2}$$

Next, the PEC regeneration ability of the LDH biosensor was also evaluated, as shown in Fig. 4B. In the presence of 100 μM L-lactate, PEDOT-TiONWs|FTO without (curve a) or with illumination (curve b) nearly did not produce any redox peaks. On the contrary, NAD^+|LDH|PEDOT-TiONWs|FTO without (curve c) and with (curve d) illumination has displayed anodic peaks. The latter (curve d) is much larger than the former due to the co-contribution from both PEC and EC oxidation of NADH to NAD^+. In summary, both the PEC and EC biosensor can

catalytically amplify the detection signal of L-lactate. Nevertheless, the electrochemical oxidation of NADH only occurs at ~0.54 V, at which some interferences could be oxidized simultaneously, leading to the poor selectivity of the sensor.

3.8. PEC characterization of the LDH biosensor assembly

The photocurrent signals under intermittent visible light were also applied to verify the assembly of the LDH biosensor. As displayed in Fig. 5A, TiONWs|FTO (curve a) generated a relatively small photocurrent, which is probably due to the large bandgap of TiONWs and facile recombination of photo-generated carriers. As expected, PEDOT-TiONWs|FTO (curve b) produced a much larger (~2.2 times) photocurrent compared with TiONWs|FTO, mainly due to the excellent PEC and electrochemical properties of PEDOT as follows: the formation of heterojunction between PEDOT and TiONWs effectively promoted the absorption of visible light, facilitated the separation of photo-generated carriers, increased the electrical conductivity and enlarged the surface area. The photocurrent at PEDOT-TiONWs|FTO electrode was only slightly enhanced after 100 μM lactate (curve c) was added into the test solution, demonstrating the stability of lactate against photo-generated hole oxidation. On the contrary, the photocurrent at PEDOT-TiONWs|FTO increased significantly after the addition of 100 μM NADH (curve d), indicating that photo-generated holes can very easily oxidize NADH to regenerate NAD^+. This phenomenon verified the possibility of our PEC system to realize the recycling of coenzyme NAD^+ for signal amplification. Among all the modified electrodes, NAD^+|LDH|PEDOT-TiONWs|FTO (curve e) in 0.1M PBS exhibited the least photocurrent, mainly due to the strong steric hindrance of the biomolecules, which prevented the movement of photo-generated electrons to FTO and increased the recombination probability of electron-hole couple.

3.9. The catalytic reaction mechanism of the PEC biosensing

The construction and PEC reaction mechanism of NAD^+|LDH|PEDOT-TiONWs|FTO are shown in Scheme 1, equations (1), (3) and (4). Under visible light excitation, the electrons on the highest occupied molecular orbital (HOMO) of PEDOT were transited to its lowest unoccupied molecular orbital (LUMO). Because the conduction band (CB) of TiONWs is lower than that of the LUMO of PEDOT, electrons in the LUMO will transfer to the CB of TiONWs. After applying a positive voltage of 0.2 V, the electrons were attracted to the FTO substrate, which could reduce photo-generated electron-hole recombination and thereby increase the photocurrent response. Subsequently, LDH converted lactate to pyruvate (Equation (1)) with the aid of coenzyme NAD^+, while NAD^+ received electrons and hydrogen to produce NADH. Meanwhile, the photo-generated holes (h^+) on the VB of TiONWs were transferred to the HOMO of PEDOT to oxidize NADH back to NAD^+ to complete a cycle (Equations (3) and (4)). In brief, increasing the lactate concentraion would generate more NADH, consume more h^+ and enhance

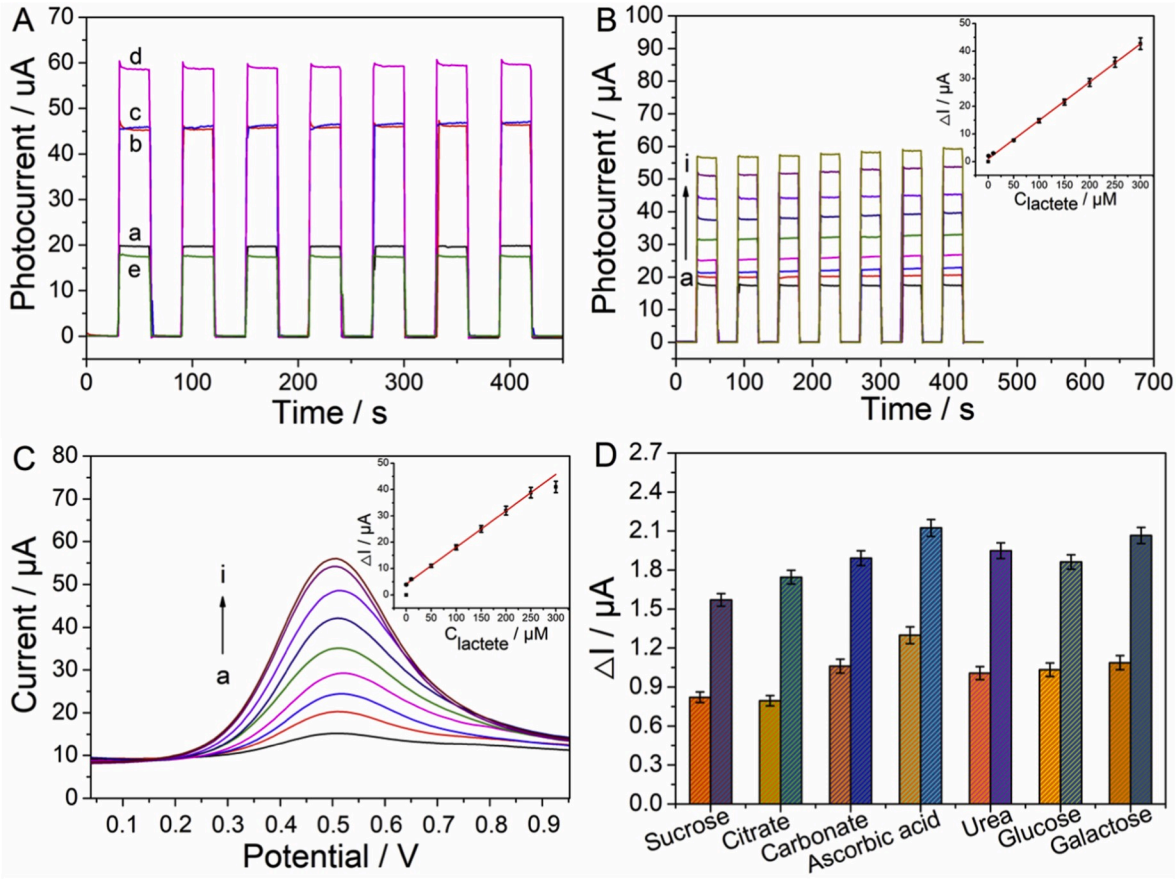

Fig. 5. (A) Photocurrent responses of (a) TiONWs|FTO, (b) PEDOT-TiONWs|FTO, (c) PEDOT-TiONWs|FTO in the presence of 100 μM L-lactate, (d) PEDOT-TiONWs|FTO in the presence of 100 μM NADH, (e) NAD^+|LDH|PEDOT-TiONWs|FTO in 0.1 M PBS (pH = 7.4); (B) Photocurrent responses of NAD^+|LDH|PEDOT-TiONWs|FTO in 0.1 M PBS (pH = 7.4) containing 0, 0.5, 10, 50, 100, 150, 200, 250 and 300 μM (a–i) of L-lactate at a potential of 0.2 V, inset is the calibration plot of photocurrent *vs* L-lactate concentration; (C) Differential pulse voltammograms (DPV) of NAD^+|LDH|PEDOT-TiONWs|FTO in 0.1 M PBS containing 0, 0.2, 10, 50, 100, 150, 200, 250 and 300 μM (a–i) of L-lactate in 0.1 M PBS (pH = 7.4), inset is the calibration plot of DPV peak current change (Δ*I*) *vs* L-lactate concentration; (D) Anti-interference study of the PEC (left) and EC (right) biosensors in 50 μM of lactate in PBS (0.1 M, pH = 7.4) containing 50 μM of sucrose, citrate, carbonate, ascorbic acid, urea, glucose and galactose, respectively, the error bars were obtained from the standard deviations of three independent measurements.

Table 1
Analytical performance of some PEC and EC biosensors for L-lactate.

LDH-based biosensors	Linear Range (μM)	Detection limit (μM)	References
MWCNT-TiO_2|LDH|NAD^+|ITO	0.5–120	0.1	Liu et al. (2015)
TiONT[a]-PANI-GNP|LDH|NAD^+|ITO	0.5–210	0.15	Zhu et al. (2016)
TiONT-PANI|LDH|NAD^+|ITO	1–180	0.55	Zhu et al. (2016)
Fe_3O_4|MWCNTs|LDH|NAD^+	50–500	5.0	Teymourian et al. (2012)
Au|Nano ZnO|LDH	0.2–0.8	0.0047	Nesakumar et al. (2014)
MWCNT-CHIT[b]-LDH	5–120	0.76	Tsai et al. (2007)
Nano-TiO_2–LDH|GCE	1–20	0.4	Cheng et al. (2008)
Sol–gel|PVA[c]-LDH|Au electrode	2–30	0.80	Di et al. (2007)
Polysulfone|MWCNT|LDH|SPCE[d]	1–20	0.37	Pérez et al. (2012)
LDH|Au-EVIMC[e]-TiNTs-PANI|ITO	0.55–5.55	0.165	Cheng et al. (2018)
NAD^+|LDH|PEDOT-TiONWs|FTO[f]	0.2–250	0.1	This work
NAD^+|LDH|PEDOT-TiONWs|FTO[g]	0.5–300	0.08	This work

[a] Titanate nanotube.
[b] chitosan.
[c] Poly(vinyl alcohol).
[d] Screen-printed carbon electrode.
[e] 1-ethyl-3-vinylimidazolium chloride.
[f] EC biosensor.
[g] PEC biosensor.

photocurrent, thereby resulting in the highly sensitive quantitative determination of lactate.

$$TiONWs - PEDOT \xrightarrow{illumination} h^+ + e^- \quad \text{Equation 3}$$

$$NADH - 2e^- \xrightarrow{h^+} NAD^+ + H^+ \quad \text{Equation 4}$$

3.10. Analytical performance of the PEC and EC biosensing

In this work, NAD^+|LDH|PEDOT-TiONWs|FTO sensor was used for both PEC and EC detection of L-lactate, and the current-time I(i-t) plot was constructed accordingly. All experiments were performed under optimized conditions, and the specific optimization was described in detail in the supplementary materials, as shown in Fig. S1. (Optimized parameters: applied voltage was 0.2 V, [LDH] was 5 mg mL^{-1} and [NAD^+] was 15 mM, all the solutions were prepared using pH 7.4 PBS). As shown in Fig. 5B, the PEC biosensor exhibited a fast response to the intermittent excitation light and stable photocurrent could be obtained within a short time. Under the optimal conditions (Fig. S1), the photocurrent of the PEC biosensor increased with the L-lactate concentration. A linear relationship between ΔI ($\Delta I = I–I_0$, where I and I_0 represent the photocurrent in the presence and absence of lactate) and L-lactate concentration was observed in Fig. 5B (inset). The sensor exhibited a linear relationship in the 0.5–300 μM (correlation coefficient was 0.993) range with a sensitivity of 0.1386 ± 0.0053 μA μM^{-1} (n = 6) and a detection limit of 0.08 μM ± 0.0032 μM ($S/N = 3$, all errors denoted the 95% confidence intervals). The comprehensive performance of NAD^+|LDH|PEDOT-TiONWs|FTO biosensor is superior to that of most EC and PEC biosensors previously reported, as shown in Table 1. The superior performance can be attributed to the strong regeneration of NADH by the photo-induced holes, and the special features of the PEDOT-TiONWs hetero-junction.

Differential pulse voltammetry (DPV) was used to study the analytical performance of the EC biosensor. Fig. 5C shows the differential pulse voltammograms of NAD^+|LDH|PEDOT-TiONWs|FTO sensor at increasing concentrations of L-lactate in 0.1 M PBS (pH 7.4). The current difference ΔI ($\Delta I = I–I_0$, where I and I_0 represent the currents in the presence and absence of L-lactate) enhanced proportionally with the increase in the L-lactate concentration. The calibration plot (the inset of Fig. 5C) exhibited a linear range from 0.2 to 250 μM (correlation coefficient was 0.995), a sensitivity of 0.1345 ± 0.0065 μA μM^{-1} (n = 6) and a detection limit of 0.100 μM ± 0.0042 μM ($S/N = 3$, all errors represent the 95% confidence intervals), which are similar to that of the PEC biosensor because of the strong electrocatalytic capability and high conductivity of the PEDOT-TiONWs hetero-junction.

Moreover, seven interfering substances including sucrose, citrate, carbonate, ascorbic acid, urea, glucose and galactose were added to the lactate sample to detect the anti-interference ability of the PEC and EC biosensors. The photocurrent only increased by 3.1 (±0.115)%, 3.0 (±0.105)%, 4.0 (±0.144)%, 4.9 (±0.191)%, 3.8 (±0.152)%, 3.9 (±0.160)% and 4.1 (±0.176)% compared to the original PEC current after the addition of 50 μM of each interference substance to 50 μM of lactate in PBS. On the other hand, for the EC biosensor, the current signal increased by 5.4 (±0.216)%, 6.0 (±0.276)%, 6.5 (±0.299)%, 7.3 (±0.314)%, 6.7 (±0.281)%, 6.4 (±0.243)%, and 7.1 (±0.312)% as shown in Fig. 5D (N = 6 in all the cases, all errors represent the 95% confidence intervals). Apparently, the current changes caused by the oxidation of the above interferening species can be ignored relative to the EC and PEC current signals. The anti-interference of the EC biosensor is not as good as that of the PEC biosensor and it can be attributed to the relatively high oxidation potential (0.54 V) of NADH that can oxidize more interference substances than the applied voltage during PEC sensing (0.2 V).

Good repeatability of the PEC biosensor was confirmed from the relative standard deviation (RSD) of 4.1% obtained from 6 consecutive determinations of an L-lactate sample (100 μM) using one PEC biosensor, and that of the EC biosensor was found to be 5.2%. In order to assess the reproducibility, six identical biosensors (N = 6) were used to determine the L-lactate sample (100 μM) under same experimental conditions. A RSD of 4.6% and 5.4% was obtained for PEC and EC detection respectively indicating the excellent analytical reproducibility of the biosensor.

In addition, the PEC and EC biosensors stored at 4 °C for 1 week, 2 weeks and 4 weeks, still exhibited 96.7 (±2.88)%/96.1 (±3.25)%, 94.5 (±3.59)%/93.5 (±3.43)% and 88.1 (±3.91)%/86.8 (±3.72)% of the initial current signals at the 95% confidence intervals, confirmed the good long-term stability of the biosensors.

3.11. Application of the proposed biosensors in human serum samples

As shown in Table 2, the PEC and EC biosensors were used to detect the lactate content in the practical samples, and the results were also compared with the standard spectrophotometric results. The serum samples were firstly centrifuged at 2000 rpm for 30 min and the

Table 2
Determination of lactate in human serum samples with standard spectrophotometry, PEC and EC biosensors.

Analytical technique	Initial (mM)	Added (mM)	Found (mM)	Recovery (%)	Standard deviation (mM)
Spectrophotometry (Ref. Method)	0.206	–	–	100.0	0.0089
		0.02	0.229	101.2	0.0078
PEC biosensors	0.210	–	–	101.9	0.0111
		0.02	0.223	98.5	0.0082
EC biosensors	0.198	–	–	96.1	0.0109
		0.02	0.220	97.4	0.0092

All uncertainties denote the 95% confidence intervals. All results are the average of six determinations.

supernatant was then collected and diluted 10-fold in PBS. Using the PEC and EC biosensors, the lactate concentrations in the serum samples were detected to be ~0.210 (RSD = 5.3%, n = 6) and 0.198 (RSD = 5.5%, n = 6) mM respectively. The concentration of lactate in the same serum samples was found to be ~0.206 (RSD = 4.3%, n = 6) mM by the standard spectrophotometry. The above results have shown the good consistency between the three methods, indicating that both the PEC and EC biosensors are promising techniques for practical application.

4. Conclusion

In summary, a PEDOT-TiONWs composite was prepared and its surface morphology, structure, composition and conductivity were then characterized by SEM, EDX, XRD, FT-IR, XPS, UV–visible and EIS, respectively. Following this, LDH and coenzyme NAD^+ were modified on the PEDOT-TiONWs|FTO electrode through the amide bond to construct a biosensor, which could be used for both PEC and EC biosensing. PEDOT-TiONWs exhibited a strong PEC and EC responses, excellent biocompatibility, large surface area and high conductivity. The cyclic catalytic mechanism of the PEC and EC sensors were confirmed by the experimental results. Under optimal conditions, the PEC biosensor exhibited a sensitivity of $0.1386 \pm 0.0053\ \mu A\ \mu M^{-1}$ and detection limits of 0.08 μM ± 0.0032 μM in the 0.5–300 μM linear range, which are superior over most of the other lactate sensors. The EC biosensor also showed a comparable analytical performance as that of PEC biosensor except its relatively poor anti-interference behavior due to the high oxidation potential of NADH that can possibly oxidize the interferences to produce larger false signals.

Declaration of competing interest

The authors declare that they have no known competing financial interests or personal relationships that could have appeared to influence the work reported in this paper.

CRediT authorship contribution statement

Hejie Zheng: Conceptualization, Methodology, Investigation, Writing - original draft, Software. **Si Zhang:** Supervision, Software. **Xiaoqiang Liu:** Conceptualization, Methodology, Funding acquisition, Writing - original draft. **Yanmei Zhou:** Supervision. **Subbiah Alwarappan:** Methodology, Supervision, Writing – review & editing.

Acknowledgements

This work was financially supported by National Natural Science Foundation of China (No. U1504215, 21576071, 21776061), International Science and Technology Cooperative Project funded by The Department of Science and Technology of Henan Province (172102410042), the program for Science & Technology Innovation Talents in Universities of Henan Province (19HASTIT037) and the program for Science & Technology Innovation Team in Universities of Henan Province (19IRTSTHN029).

Appendix A. Supplementary data

Supplementary data to this article can be found online at https://doi.org/10.1016/j.bios.2020.112234.

References

Celik, A.C., Ozturk, F., Erden, P.E., Kacar, C., Kilic, E., 2015. Electroanalysis 27, 2820–2828.
Chen, Y., Kim, H.C., McVittie, J., Ting, C., Nishi, Y., 2010. Nanotechnology 21, 185303.
Chen, L., Liu, W., Su, X., Xiao, S., Xie, H., Uher, C., Tang, X., 2017. Synth. Met. 229, 65–71.
Cheng, J., Di, J., Hong, J., Yao, K., Sun, Y., Zhuang, J., Xu, Q., Zheng, H., Bi, S., 2008. Talanta 76, 1065–1069.
Cheng, H., Hu, C., Ji, Z., Ma, W., Wang, H., 2018. Biosens. Bioelectron. 118, 97–101.
Chong, B.H., Zhu, W., Hou, X.H., 2017. J. Mater. Chem. A. 5, 6233–6244.
Cui, W., Bai, H., Qu, K., Wang, F., Guan, P., Xu, D., Fan, W., Shi, W., 2019. Energy Technol. 7, 1801128.
Di, J., Cheng, J., Xu, Q., Zheng, H., Zhuang, J., Sun, Y., Wang, K., Mo, X., Bi, S., 2007. Biosens. Bioelectron. 23, 682–687.
Dong, W., Li, H., Xi, J., Mu, J., Huang, Y., Ji, Z., Wu, X., 2017. J. Alloys Compd. 724, 280–286.
Dong, J., Ma, G., Sui, L., Wei, M., Satheesh, V., Zhang, R., Ge, S., Li, J., Zhang, T.E., Wittwer, C., Jessen, H.J., Zhang, H., An, G.Y., Chao, D.Y., Liu, D., Lei, M., 2019. Mol. Plant 12, 1463–1473.
Gao, X., Niu, S., Ge, J., Luan, Q., Jie, G., 2020. Biosens. Bioelectron. 147, 111778.
Ghosh, S., Remita, H., Ramos, L., Dazzi, A., Deniset-Besseau, A., Beaunier, P., Goubard, F., Aubert, P.H., Brisset, F., Remita, S., 2014. New J. Chem. 38, 1106–1115.
Ghosh, S., Mallik, A.K., Basu, R.N., 2018. Sol. Energy 159, 548–560.
Guo, D., Wang, L., Wang, X., Xiao, Y., Wang, C., Chen, L., Ding, Y., 2020. Sensor. Actuator. B Chem. 305, 127488.
Gupta, P., Bharti, A., Kaur, N., Singh, S., Prabhakar, N., 2018. J. Electroanal. Chem. 813, 102–108.
He, J., Zhang, C., Dai, H., Liu, H., Zhang, X., Yang, J., Chen, X., Zhu, Y., Wang, D., Qi, X., Li, W., Wang, Z., An, G., Yu, N., He, Z., Wang, Y.F., Xiao, Y., Zhang, P., Wang, E., 2019. Mol. Plant 12, 1561–1576.
Ibupoto, Z.H., Shah, S.M., Khun, K., Willander, M., 2012. Sensors 12, 2456–2466.
Janaky, C., Bencsik, G., Racz, A., Visy, C., de Tacconi, N.R., Chanmanee, W., Rajeshwar, K., 2010. Langmuir 26, 13697–13702.
Jiang, F., Yue, R., Du, Y., Xu, J., Yang, P., 2013. Biosens. Bioelectron. 44, 127–131.
Kim, J.I., Zhang, X., Pascuzzi, P.E., Liu, C.J., Chapple, C., 2020. New Phytol. 225, 154–168.
Lei, Y., Luo, N., Yan, X., Zhao, Y., Zhang, G., Zhang, Y., 2012. Nanoscale 4, 3438–3443.
Lei, S., Liu, X., Zhang, X., Huang, Z., He, C., Yang, Y., 2019. Mater. Today Commun. 20, 100549.
Li, C., Xu, J., Wu, Y., Zhang, Y., Zhang, C., Lei, W., Hao, Q., 2018. J. Electroanal. Chem. 824, 52–59.
Li, L., Liu, X., Yang, L., Zhang, S., Zheng, H., Tang, Y., Wong, D.K.Y., 2019. Biosens. Bioelectron. 142, 111525.
Ling, H., Zhang, R., Ye, X., Wen, Z., Xia, J., Lu, X., 2019. Sol. Energy 190, 63–68.
Liu, X., Yan, R., Zhu, J., Huo, X., Wang, X., 2015. Electrochim. Acta 173, 260–267.
Liu, P.P., Liu, X., Huo, X.H., Tang, Y., Xu, J., Ju, H., 2017a. ACS Appl. Mater. Interfaces 9, 27185–27192.
Liu, X., Huo, X., Liu, P., Tang, Y., Xu, J., Ju, H., 2017b. Biosens. Bioelectron. 92, 171–178.
Lv, M., Yang, L., Wang, X., Cheng, X., Song, Y., Yin, Y., Liu, H., Han, Y., Cao, K., Ma, W., Qi, G., Li, S., 2019. RSC Adv. 9, 40694–40707.
M, P.R., Berchmans, S., 2019. Sci. Rep. 9, 1–13.
Madhuvilakku, R., Alagar, S., Mariappan, R., Piraman, S., 2020. Anal. Chim. Acta 1093, 93–105.
Monošík, R., Streďanský, M., Greif, G., Šturdík, E., 2012. Food Contr. 23, 238–244.
Munusamy, S., Suresh, R., Giribabu, K., Manigandan, R., Praveen Kumar, S., Muthamizh, S., Bagavath, C., Stephen, A., Kumar, J., Narayanan, V., 2019. Arab. J. Chem. 12, 3565–3575.
Nesakumar, N., Thandavan, K., Sethuraman, S., Krishnan, U.M., Rayappan, J.B., 2014. J. Colloid Interface Sci. 414, 90–96.
Parra, A., Casero, E., Vazquez, L., Pariente, F., Lorenzo, E., 2006. Anal. Chim. Acta 555, 308–315.
Pérez, S., Sánchez, S., Fàbregas, E., 2012. Electroanalysis 24, 967–974.
Piano, M., Serban, S., Pittson, R., Drago, G.A., Hart, J.P., 2010. Talanta 82, 34–37.
Rajesh, M., Raj, C.J., Kim, B.C., Manikandan, R., Kim, S.-J., Park, S.Y., Lee, K., Yu, K.H., 2016. RSC Adv. 6, 110433–110443.
Rajesh, M., Raj, C.J., Manikandan, R., Kim, B.C., Park, S.Y., Yu, K.H., 2017. Mater. Today Energy 6, 96–104.
Rathee, K., Dhull, V., Dhull, R., Singh, S., 2016. Biochem Biophys Rep 5, 35–54.
Samu, G.F., Visy, C., Rajeshwar, K., Sarker, S., Subramanian, V.R., Janáky, C., 2015. Electrochim. Acta 151, 467–476.
Shao, D., Zheng, L., Feng, D., He, J., Zhang, R., Liu, H., Zhang, X., Lu, Z., Wang, W., Wang, W., Lu, F., Dong, H., Cheng, Y., Liu, H., Zheng, R., 2018. J. Mater. Chem. A. 6, 4032–4039.
Shuai, H.-L., Huang, K.-J., Chen, Y.-X., 2016. J. Mater. Chem. B. 4, 1186–1196.
Tang, Y., Chai, Y., Liu, X., Li, L., Yang, L., Liu, P., Zhou, Y., Ju, H., Cheng, Y., 2018. Biosens. Bioelectron. 117, 224–231.
Teymourian, H., Salimi, A., Hallaj, R., 2012. Biosens. Bioelectron. 33, 60–68.
Tsai, Y.-C., Chen, S.-Y., Liaw, H.-W., 2007. Sens. Actuators B Chem. 125, 474–481.
Wang, P., Du, Y., Li, Y., Ren, D., Song, C.P., 2010. Plant Cell 22, 2981–2998.
Wang, G., Wang, H., Ling, Y., Tang, Y., Yang, X., Fitzmorris, R.C., Wang, C., Zhang, J.Z., Li, Y., 2011. Nano Lett. 11, 3026–3033.
Wang, Y., Chu, W., Wang, S., Li, Z., Zeng, Y., Yan, S., Sun, Y., 2014. ACS Appl. Mater. Interfaces 6, 20197–20204.
Wang, J., Wang, X., Yan, J., Tan, Q., Liang, G., Qu, S., Zhong, Z., 2018a. Materials 11, 1791.
Wang, Y.H., Xia, H., Huang, K.J., Wu, X., Ma, Y.Y., Deng, R., Lu, Y.F., Han, Z.W., 2018b. Mikrochim. Acta 185, 502.
Wu, L.-N., Zhong, J.-P., Waqas, M., Jiang, Z., Fan, Y.-J., Sun, Y., Li, J., Chen, W., 2019. Electrochim. Acta 318, 837–846.

Yang, L., Liu, X., Li, L., Zhang, S., Zheng, H., Tang, Y., Ju, H., 2019. Biosens. Bioelectron. 142, 111487.
Zeng, B., Chen, Y., Bai, J., 2019. J. Mater. Sci. Mater. Electron. 30, 17706–17714.
Zhang, S., Zhang, S., Peng, B., Wang, H., Yu, H., Wang, H., Peng, F., 2014. Electrochem. Commun. 40, 24–27.
Zhao, Y.G., Yan, X.Q., Kang, Z., Fang, X.F., Zheng, X., Zhao, L.Q., Du, H.W., Zhang, Y., 2014. J. Nanoparticle Res. 16, 2398.
Zhao, Y., Fang, X., Gu, Y., Yan, X., Kang, Z., Zheng, X., Lin, P., Zhao, L., Zhang, Y., 2015. Colloids Surf. B Biointerfaces 126, 476–480.
Zhu, J., Huo, X., Liu, X., Ju, H., 2016. ACS Appl. Mater. Interfaces 8, 341–349.
Łapkowski, M., Proń, A., 2000. Synth. Met. 110, 79–83.